

Article

Characterization of PROPPIN-Phosphoinositide Binding and Role of Loop 6CD in PROPPIN-Membrane Binding

Ricarda A. Busse,¹ Andreea Scacioc,¹ Roswitha Krick,² Ángel Pérez-Lara,¹ Michael Thumm,² and Karin Kühnel^{1,*}

¹Department of Neurobiology, Max Planck Institute for Biophysical Chemistry, Göttingen, Germany; and ²Institute of Cellular Biochemistry, University Medicine, Georg-August University, Göttingen, Germany

ABSTRACT PROPPINs (β -propellers that bind polyphosphoinositides) are a family of PtdIns3P- and PtdIns(3,5)P₂-binding proteins that play an important role in autophagy. We analyzed PROPPIN-membrane binding through isothermal titration calorimetry (ITC), stopped-flow measurements, mutagenesis studies, and molecular dynamics (MD) simulations. ITC measurements showed that the yeast PROPPIN family members Atg18, Atg21, and Hsv2 bind PtdIns3P and PtdIns(3,5)P₂ with high affinities in the nanomolar to low-micromolar range and have two phosphoinositide (PIP)-binding sites. Single PIP-binding site mutants have a 15- to 30-fold reduced affinity, which explains the requirement of two PIP-binding sites in PROPPINs. Hsv2 bound small unilamellar vesicles with a higher affinity than it bound large unilamellar vesicles in stopped-flow measurements. Thus, we conclude that PROPPIN membrane binding is curvature dependent. MD simulations revealed that loop 6CD is an anchor for membrane binding, as it is the region of the protein that inserts most deeply into the lipid bilayer. Mutagenesis studies showed that both hydrophobic and electrostatic interactions are required for membrane insertion of loop 6CD. We propose a model for PROPPIN-membrane binding in which PROPPINs are initially targeted to membranes through nonspecific electrostatic interactions and are then retained at the membrane through PIP binding.

INTRODUCTION

PROPPINs (β -propellers that bind polyphosphoinositides) are a family of PtdIns3P- and PtdIns(3,5)P₂-binding proteins that are important in autophagy (1,2). They are conserved from yeast to humans and contain a characteristic FRRG motif, which is essential for phosphoinositide (PIP) binding (2–4). *Saccharomyces cerevisiae* has three highly homologous PROPPINs—Atg18, Atg21, and Hsv2 (homologous with swollen vacuole phenotype 2)—and PtdIns3P binding is needed for their autophagic functions.

Atg18 is a core autophagy protein required for macroautophagy (4–6). During macroautophagy, cytosolic content is nonspecifically taken up in double-membraned autophagosomes, which then fuse with the vacuole, where they are degraded. Atg18 localizes PtdIns3P-dependent of the preautophagosomal structure (PAS), the site at which autophagosome formation originates (7,8). Human WIPI2b (WD-40 repeat containing protein that interacts with PtdIns) is an ortholog of Atg18 (9). WIPI2b recruits the essential Atg12-Atg5-Atg16L1 complex to form autophagosomes by interacting with Atg16L1 (10).

In addition to macroautophagy, Atg18 is also needed for yeast-specific autophagic subtypes, including the cytoplasm-to-vacuole targeting pathway (Cvt), which delivers

specific hydrolytic enzymes to the vacuole, and piecemeal microautophagy of the nucleus (PMN), where parts of the nucleus are pinched off and degraded in the vacuole (4–6,11). PtdIns(3,5)P₂ binding mediates Atg18 targeting to the vacuole, where it has a regulatory role as a component of the Fab1-containing PtdIns3P 5-kinase complex (12,13) and is required for retrograde transport from the vacuole to the Golgi (2). In contrast, Atg21 is needed for the Cvt pathway and PMN, but only partially affects macroautophagy (3,11,14). Recently, it was shown that Atg21 organizes the site of Atg8 lipidation at the PAS through PtdIns3P binding and its interactions with Atg16 and Atg8 (15). However, for Hsv2, only a requirement for efficient PMN has been reported to date (8). The three yeast PROPPINs also localize to endosomes in a PtdIns3P-dependent manner, but their endosomal functions are unknown (8).

The Hsv2 crystal structures led to new insights into the PIP-binding mode of PROPPINs (16–18). PROPPINs fold as seven-bladed β -propellers with two PIP-binding sites on the rim of each propeller. Each of the two FRRG arginines is part of one PIP-binding site. In addition to the two PIP-binding sites, loop 6CD, which connects the two outer strands of blade 6, is important for membrane binding of PROPPINs (17). Recently, it was reported that phosphorylation of loop 6CD has a regulatory role in membrane targeting of PROPPINs because phosphorylation decreases membrane binding of Atg18 (19).

Our goal was to gain further insights into the mechanism of membrane binding of this PIP effector family by

Submitted September 25, 2014, and accepted for publication March 24, 2015.

*Correspondence: kkuehne@gwdg.de

Ricarda A. Busse and Andreea Scacioc contributed equally to this work.

Editor: Joseph Falke.

© 2015 by the Biophysical Society
0006-3495/15/05/2223/12 \$2.00



<http://dx.doi.org/10.1016/j.bpj.2015.03.045>

combining a range of biophysical, computational, and cell biological methods. We performed isothermal titration calorimetry (ITC) measurements with the three yeast PROPPIN family members (Atg18, Atg21, and Hsv2). PROPPINs bind PtdIns3P and PtdIns(3,5)P₂ with high affinities in the nanomolar to low-micromolar range. Stopped-flow kinetic measurements suggest that membrane targeting is initially driven by nonspecific electrostatic interactions, and PROPPINs are then retained at the membrane through PIP binding. We used mutagenesis studies and MD simulations to analyze membrane binding of loop 6CD, and found that both hydrophobic and electrostatic interactions are important for membrane association. We also show that loop 6CD is the region of the protein that inserts most deeply into the lipid bilayer, leaving a large portion of the surface available for PROPPIN-protein interactions.

MATERIALS AND METHODS

Protein expression and purification

Saccharomyces cerevisiae Hsv2 (ScHsv2) and its alanine mutants were expressed as GST-fusion proteins. The GST-tag was cleaved off during purification as previously described (16). *Kluyveromyces lactis* Hsv2 (KIHsv2) point mutants were prepared with the QuikChange Lightning Multi Site-Directed Mutagenesis Kit (Agilent Technologies, Santa Clara, CA) (Table S1 in the Supporting Material). KIHsv2^{loop6CD-ScHsv2} consists of KIHsv2 residues 1–254 and 277–339, which are linked through ScHsv2 loop 6CD residues 300–338. A synthetic gene encoding KIHsv2^{loop6CD-ScHsv2} was purchased from Mr. Gene (Regensburg, Germany) and cloned into pET-28a (Merck Millipore, Bedford, MA) using NdeI and XhoI cleavage sites (Table S2). The KIHsv2^{Δloop6CD-GS} construct KIHsv2(1–256)-(GS)₄G-(275–339) was generated by PCR and cloned into pET-28a with NdeI and XhoI restriction sites. Wild-type and KIHsv2 mutants were expressed as N-terminal His₆-tagged proteins and purified as previously described (16).

Genes encoding *Pichia angusta* Atg18 (PaAtg18) (UniProt entry Q5QA94) and *Kluyveromyces lactis* Atg21 (KlAtg21) (NCBI reference sequence XP_455047) were codon optimized for *E. coli* expression, chemically synthesized, and cloned into the pET-28a vector between NdeI and XhoI restriction sites. Proteins were expressed with an N-terminal His₆-tag in *E. coli* BL21(DE3) in ZYM-5052 autoinducing medium (20) for 3 h at 37°C, and then overnight at 25°C (PaAtg18) or 22°C (KlAtg21). After harvesting, the cells were resuspended in 20 mM imidazole, 0.5 M NaCl, and 50 mM HEPES pH 7.5.

Bacteria were lysed in a microfluidizer M-110L (Microfluidics, Westwood, MA) and spun at 14,000 rpm for 1 h at 4°C. Supernatant was applied onto a 5 mL HisTrap column (GE Healthcare, Freiburg, Germany) using an Äkta FPLC system. Proteins were eluted with a gradient up to 500 mM imidazole. Samples were concentrated and loaded onto a Superdex 75 Hi-Load 16/60 column (GE Healthcare) with 300 mM NaCl, 30 mM HEPES pH 7, and 1 mM dithiothreitol as the gel filtration buffer. PaAtg18 and KlAtg21 containing N-terminal His₆-tags were concentrated and flash-frozen in liquid nitrogen.

Crystallization and structure determination

KIHsv2^{Δloop6CD-GS} was crystallized using the hanging-drop method in 24-well Linbro plates at 20°C. For crystallization, 2 μL of 20 mg/ml protein was mixed with 2 μL of precipitant consisting of 14% (wt/V) PEG 3350, 0.2 M MgCl₂, 0.1 M Tris pH 9.0. Crystals were transferred into a cryoprotectant composed of 10% (wt/V) xylitol, 10% (wt/V) sucrose, 14% PEG

3350, 0.2 M MgCl₂, and 0.1 M Tris pH 9.0, and flash-cooled in liquid nitrogen. Diffraction data were collected at SLS beamline X10SA (Swiss Light Source, Paul Scherrer Institute, Villigen, Switzerland) at 100 K. Data were processed with the XDS software package (21). The structure was determined by molecular replacement using MOLREP (22), with wild-type KIHsv2 used as the search model (PDB ID: 4AV9) (16). Refinement was done with PHENIX (23), and COOT (24) was used for model building. Figures were prepared with PyMOL (25). The coordinates and structure factors have been deposited in the PDB under accession code 4V16.

Small unilamellar vesicle preparation for ITC measurements and flotation assays

Small unilamellar vesicles (SUVs) were prepared using the detergent-dilution method with sodium cholate. These SUVs have an average diameter of 36 nm (26). Stock solutions of lipids were prepared with chloroform (Table S3). Then, 1 mg of the lipid mixture was prepared and air dried. SUVs for ITC measurements consisted of 72% (wt/wt) phosphatidylcholine (PC), 24% PE, 2% Texas Red-PE, and either 2% PtdIns3P or 2% PtdIns(3,5)P₂. Liposomes for liposome flotation assays were composed of 74% (wt/wt) PC, 23% phosphatidylethanolamine (PE), 2% Texas Red-PE, and 1% PIP.

Dried lipids were resuspended in 150 μL HP150 (150 mM KCl, 20 mM HEPES pH 7.4) buffer containing 3% (wt/V) sodium cholate. Cholate was removed by size-exclusion chromatography using a self-packed column filled with 0.5 g of Sephadex G50 (Sigma-Aldrich, Munich, Germany) resuspended in HP150 buffer. Liposome-containing fractions were pooled and stored at 4°C for no longer than several days (26,27).

ITC measurements

Proteins were dialyzed into HP150 buffer. Protein concentrations were determined by measuring the UV absorbance at 280 nm. Measurements were done with a VP ITC MicroCalorimeter (Malvern Instruments, Herrenberg, Germany) at 25°C. Protein was titrated into liposomes. Titrations were typically carried out with 9-fold 4 μL injections followed by 17-fold 15 μL injections. The first injection was 2 μL and was always discarded for data analysis. The protein concentration range used for measurements was 35–80 μM for wild-type proteins and 85–130 μM for the ScHsv2 alanine mutants. To determine the PIP concentration, we measured the phosphate content of liposomes using the phosphomolybdate method (26,28). We assumed that 60% of the total lipids are accessible on the surface of SUVs (26). The calculated accessible PIP concentrations were in the range of 4.5–10 μM. Data were fitted with a single-site binding model using the MicroCal Origin 7.0 software. Final values for the thermodynamic parameters are given as averages of several measurements with the standard error (SE) of measurement.

Liposome flotation assays

For liposome flotation assays, 80% (wt/V) and 30% (wt/V) Nycodenz (Progen, Heidelberg, Germany) stock solutions were prepared with HP150 buffer. Proteins were diluted with HP150 buffer. Then, 5 μL of 1.5–2 μM protein was mixed with 45 μL of liposomes, incubated for 10 min at room temperature, and mixed with 50 μL 80% (wt/V) Nycodenz. The mixture was then overlaid with 50 μL 30% Nycodenz, and 30 μL HP150 was added on top. Probes were spun at 55,000 rpm (275,000 × g) for 90 min at 4°C with a S55-S rotor in a Sorvall Discovery M150 SE analytical ultracentrifuge (Thermo Scientific, Waltham, MA). Afterward, 30 μL samples were taken starting from top of the gradient and analyzed by immunoblotting using the Penta-His HRP Conjugate antibody (Qiagen, Hilden, Germany) in a 1:2000 dilution.

Stopped-flow measurements

Vesicles were generated by mixing chloroform solutions of the different phospholipids in the desired proportions. Lipids were dried under a stream of oxygen-free nitrogen and remaining traces of organic solvent were removed under vacuum for at least 4 h. Dried lipids were resuspended in the corresponding buffers by vigorous vortexing. Then, large unilamellar vesicles (LUVs) of ~100 nm diameter were prepared by extruding rehydrated phospholipid suspensions 21 times through a 0.1 μ m polycarbonate membrane (Millipore, Bedford, MA) after five freeze-thaw cycles. SUVs were prepared as described above.

Kinetic experiments were carried out on an SX.20 stopped-flow spectrophotometer (Applied Photophysics, Leatherhead, UK) at 37°C in HP150 buffer as described previously (29). KIHsv2 (2 μ M) was mixed with equal volumes of increasing concentrations of dansyl-labeled vesicles under pseudo-first-order conditions. Vesicle concentration was calculated assuming that one vesicle is composed of 90,000 phospholipid molecules (30,31).

The excitation wavelength was set at 280 nm and a 470 nm cutoff filter was used to collect the dansyl emission at the different vesicle concentrations tested. The resulting time courses were fitted to a single-exponential function:

$$F(t) = F_0 + A_{\text{obs}} e^{-k_{\text{obs}} t},$$

where $F(t)$ equals the observed fluorescence at time t , F_0 is the final fluorescence, A_{obs} equals the amplitude, and k_{obs} is the observed rate constant. Observed rate constants were plotted as a function of vesicle concentration and fitted with the equation

$$k_{\text{obs}} = k_{\text{on}}[v] + k_{\text{off}},$$

where k_{on} represents the apparent association constant, and k_{off} is the apparent dissociation rate constant. The ratio of k_{off} to k_{on} provides the calculated apparent dissociation constant (K_d).

Fluorescence microscopy

Wild-type KIHsv2 and mutants were cloned into pUG36 (32) using the BamHI and XhoI cleavage sites to generate GFP-KIHsv2 fusions under control of the *MET25* promoter. Cells were grown to 3–6 OD₆₀₀ in selection medium supplemented with 0.3 mM methionine and visualized with a DeltaVision Spectris fluorescence microscope (Applied Precision, GE Healthcare, Issaquah, WA) with a 100 \times objective and GFP (excitation wavelengths 475/28 and emission wavelengths 525/50) filter set. Images

were deconvoluted with WoRx software (Applied Precision) and processed with Adobe Photoshop CS6.

Molecular dynamics simulations

Molecular dynamics (MD) simulations were done with the KIHsv2 structure (PDB ID: 4AV8). The GROMACS 4.5.4 simulation package was used for coarse-grained (CG) membrane self-assembly (33,34). A 1- μ s-long MD simulation of the assembled bilayer-protein system was done using the GROMACS 4.6.5 simulation package (33,34).

The last frame of the CG-MD simulation of the membrane-protein system was used to produce an atomistic-level coordinate file of the membrane-protein system with the Sugar-Pie server (35). Atomistic MD simulations were done using the GROMACS 4.6.5 simulation package together with the GROMOS96 53A6 force field (36) modified for Berger lipids (37) and SPC water (38). A production run of 100 ns was done. VMD (39) and PyMOL were used for visualization. For a detailed description, see [Supporting Material](#).

RESULTS

Analysis of the two PIP-binding sites of Hsv2

To analyze the contributions of the two PIP-binding sites, we selected the site 1 ScHsv2^{R264A} and site 2 ScHsv2^{H294A} mutants for ITC measurements. We previously showed through liposome flotation assays and cellular localization studies that these residues are essential for PIP binding of PROPPINs (16). ITC measurements were done with SUVs because we observed that LUVs precipitated during measurements, and ScHsv2 does not bind water-soluble, short-fatty-acid-chain PIP analogs (26).

Proteins were titrated into 2% PtdIns3P-containing SUVs. These SUVs had a radius of 16.7 ± 11.1 nm as determined by dynamic light scattering measurements (Fig. S2). Both mutants had much lower affinities for PtdIns3P than wild-type ScHsv2. The site 1 mutant ScHsv2^{R264A} bound almost 30 times more weakly, with a K_d of 10.9 ± 1.2 μ M, and the site 2 ScHsv2^{H294A} mutant had a 15-fold decreased affinity for PtdIns3P ($K_d = 5.9 \pm 1.6$ μ M) in comparison with wild-type ScHsv2 (Table 1; Fig. 1 A).

TABLE 1 Thermodynamic parameters for PROPPIN-PIP binding

	ScHsv2	ScHsv2 ^{R264A}	ScHsv2 ^{H294A}	KIHsv2	PaAtg18	KIAtg21
PtdIns3P						
Number of measurements	5	4	4	3	4	3
Stoichiometry ^a n PROPPIN/PtdIns3P	0.6 \pm 0.1	ND	ND	0.4 \pm 0.1	0.03 \pm 0.01	0.4 \pm 0.2
K_d (μ M)	0.40 \pm 0.05	10.9 \pm 1.2	5.9 \pm 1.6	0.50 \pm 0.07	0.29 \pm 0.09	0.86 \pm 0.18
ΔH (kJ/mol)	−89.0 \pm 7.3	ND	ND	−99.1 \pm 3.9	−101.1 \pm 22.7	−84.4 \pm 21.3
$T\Delta S$ (kJ/mol)	−53.4 \pm 8.2	ND	ND	−63.0 \pm 4.1	−63.4 \pm 23.7	−49.7 \pm 21.2
ΔG (kJ/mol)	−35.7 \pm 1.0	ND	ND	−36.0 \pm 0.4	−37.8 \pm 1.1	−34.8 \pm 0.6
PtdIns(3,5)P₂						
Number of measurements	5	—	—	3	8	4
Stoichiometry ^a n PROPPIN/PtdIns(3,5)P ₂	0.7 \pm 0.1	—	—	0.6 \pm 0.1	0.5 \pm 0.1	0.3 \pm 0.1
K_d (μ M)	0.03 \pm 0.01	—	—	0.18 \pm 0.02	0.11 \pm 0.01	1.14 \pm 0.29
ΔH (kJ/mol)	−61.6 \pm 3.5	—	—	−81.6 \pm 4.8	−147.3 \pm 5.9	−170.8 \pm 25.5
$T\Delta S$ (kJ/mol)	−17.6 \pm 4.4	—	—	−43.0 \pm 5.1	−107.4 \pm 5.9	−136.6 \pm 26.1
ΔG (kJ/mol)	−44.1 \pm 1.0	—	—	−38.5 \pm 0.4	−39.9 \pm 0.3	−34.2 \pm 0.7

ND, not determined.

^aAverage values are given with SEs.

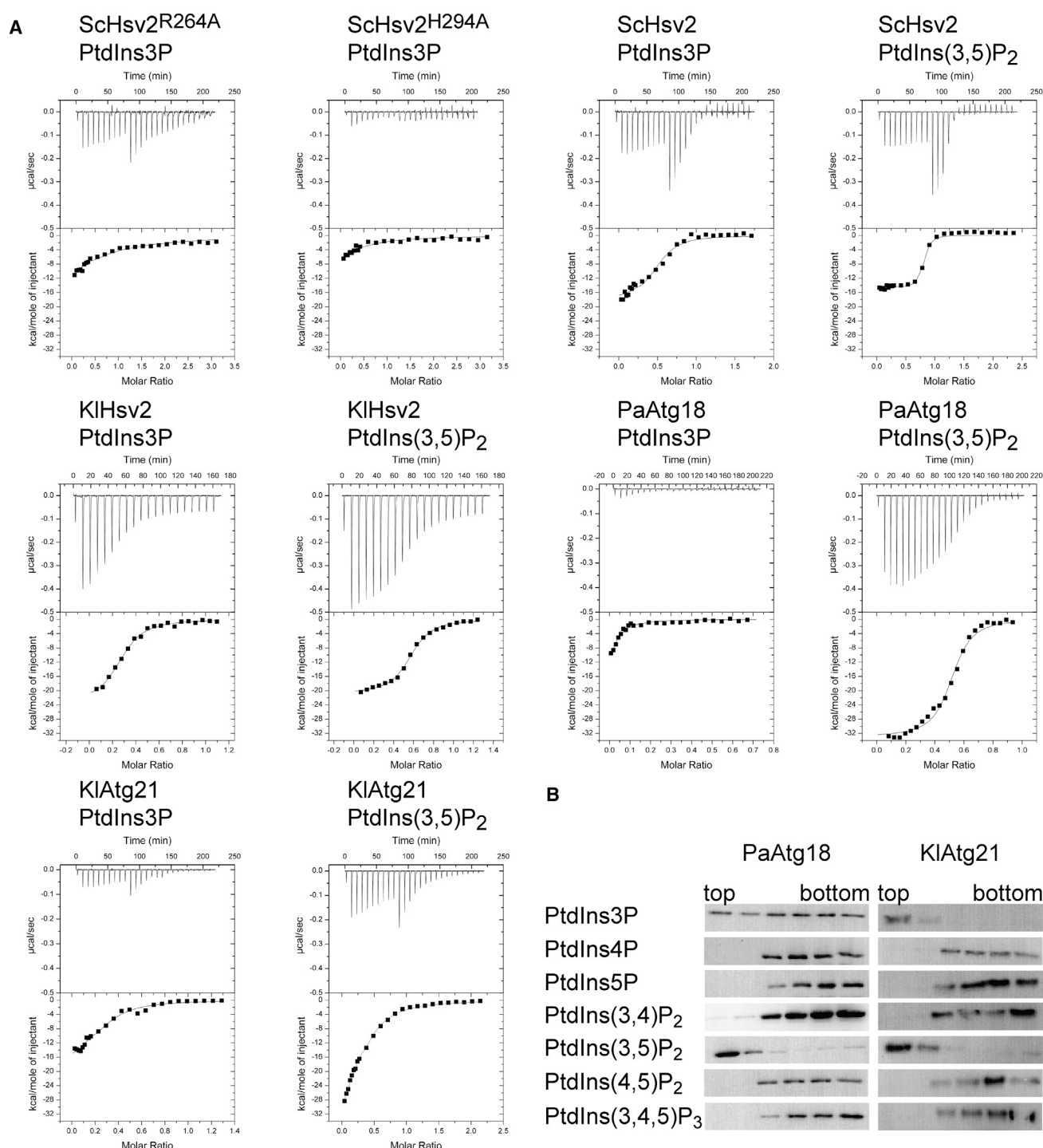


FIGURE 1 Analysis of PIP binding of PROPPINs. (A) ITC measurements of PROPPINs were done with PtdIns3P- and PtdIns(3,5)P₂-containing SUVs. Liposomes were composed of PC/PE/Texas-Red-PE/PIP (72:24:2:2, weight ratio). (B) Liposome flotation assays show the PIP binding specificities of PaAtg18 and KIAtg21. SUVs consisted of PC/PE/Texas-Red-PE/PIP (74:23:2:1, weight ratio) and the protein concentration was 2 μ M.

We further compared PtdIns(3,5)P₂ and PtdIns3P binding of wild-type ScHsv2. ScHsv2 binds with a much higher affinity to PtdIns(3,5)P₂ ($K_d = 0.03 \pm 0.01 \mu$ M). The derived stoichiometries for protein to PIP binding were

0.6 ± 0.1 for PtdIns3P and 0.7 ± 0.1 for PtdIns(3,5)P₂ binding, i.e., 1.7 PtdIns3P molecules bound to one ScHsv2 molecule, and 1.4 PtdIns(3,5)P₂ molecules bound per protein molecule. ITC measurements were also done with

KIHsv2, which shares 37% sequence identity with ScHsv2. Similarly to ScHsv2, KIHsv2 bound with a higher affinity to PtdIns(3,5)P₂ ($K_d = 0.18 \pm 0.02 \mu\text{M}$) than to PtdIns3P ($K_d = 0.50 \pm 0.07 \mu\text{M}$). The determined stoichiometries were 1.7 PtdIns(3,5)P₂ molecules and 2.5 PtdIns3P molecules binding one KIHsv2 molecule.

PIP binding of Atg18 and Atg21

Kluyveromyces lactis Atg21 and *Pichia angusta* Atg18 were used for these studies (Fig. S1) because, unlike their *S. cerevisiae* orthologs, they can be purified in high amounts from *E. coli*. First, we characterized the PIP binding specificities of the recombinant proteins by performing liposome flotation assays using SUVs containing the seven different PIP isoforms. The SUVs were composed of 1% PIP and the neutral lipids PC and PE to prevent nonspecific binding through electrostatic interactions (26).

When proteins bind to liposomes, they are found in the light top fractions. Both KlAtg21 and PaAtg21 specifically interact with PtdIns3P and PtdIns(3,5)P₂ (Fig. 1 B). KlAtg21 and PaAtg21 were expressed with N-terminal His₆-tags. The His₆-tag does not influence liposome binding because both proteins only interact with PtdIns3P and PtdIns(3,5)P₂, and not the other PIP isoform containing liposomes. However, we cannot explain why PaAtg18 is spread over all fractions for the PtdIns3P-containing liposomes, when ITC measurements show that PaAtg18 binds with high affinity to PtdIns3P ($K_d = 0.29 \pm 0.09 \mu\text{M}$). PaAtg18 has a nearly 3-fold higher affinity for PtdIns(3,5)P₂ ($K_d = 0.11 \pm 0.01 \mu\text{M}$) than for PtdIns3P (Fig. 1 A; Table 1). The stoichiometry for PtdIns(3,5)P₂ to PaAtg18 binding is 2.0, but it could not be fitted for PtdIns3P binding because the measured heat signal is weak under these conditions, which might hamper correct fitting.

In contrast, KlAtg21 has the lowest PIP affinities of all four characterized wild-type proteins, with dissociation constants in the low-micromolar range, and shows similar affinities for PtdIns3P ($K_d = 0.86 \pm 0.18 \mu\text{M}$) and PtdIns(3,5)P₂ ($K_d = 1.14 \pm 0.29 \mu\text{M}$). The derived stoichiometry is 2.5 for PtdIns3P binding to KlAtg21, and 3.3 for the interaction with PtdIns(3,5)P₂. PIP binding of all four PROPPINs has an unfavorable entropy contribution and is enthalpy driven (Table 1).

Phospholipid binding kinetics and the membrane-curvature dependency of KIHsv2 binding

We performed fluorescence resonance energy transfer (FRET)-based stopped-flow measurements to study the kinetics of PROPPIN-membrane association and to determine whether binding is membrane-curvature dependent. For this purpose, we analyzed KIHsv2 binding to LUVs and SUVs. The protein was mixed with different concentrations of 5% dansyl-DHPE (dansyl-1,2-dihexadecanoyl-*sn*-glycero-3-phosphoethanolamine)-containing liposomes. The tryptophane-to-dansyl FRET signal was measured with an excitation wavelength of 280 nm and emission was monitored at 470 nm.

We measured KIHsv2 binding to 2% PtdIns3P- and 2% PtdIns(3,5)P₂-containing SUVs. SUV preparations were characterized by dynamic light scattering measurements. The PtdIns3P-containing SUVs had a radius of 16.7 ± 11.1 nm, and PtdIns(3,5)P₂-containing SUVs had a radius of 20.0 ± 9.6 nm (Fig. S2). Rates dependent on vesicle concentration were calculated with the assumption that each SUV consists of 12,000 phospholipid molecules (40). When normalizing the association rates per surface-accessible PIP molecule, we assumed that 60% of the total lipids are localized on the liposome surface. KIHsv2 binds to both PIP isoforms containing SUVs with comparable apparent association constants and low apparent dissociation rates (Table 2; Fig. 2). The dissociation constants per surface-accessible PIP molecules are similar, with $0.6 \pm 0.5 \mu\text{M}$ for PtdIns3P and $0.7 \pm 0.4 \mu\text{M}$ for PtdIns(3,5)P₂ binding (Table 2). These values are in agreement with the ITC results, which showed a dissociation constant of $0.50 \pm 0.07 \mu\text{M}$ for PtdIns3P SUV binding. However, a higher affinity for PtdIns(3,5)P₂ binding ($K_d = 0.18 \pm 0.02 \mu\text{M}$) was observed in ITC measurements.

We further analyzed KIHsv2 binding to either 2% PtdIns3P, 2% PtdIns(3,5)P₂, or 40% dioleoyl phosphatidylserine (DOPS)-containing LUVs, which had a diameter of ~100 nm. Measurements were done with LUVs containing 40% DOPS because at lower DOPS concentrations the measured signal was too weak for a meaningful fitting of the data. No precipitation was observed during measurements. Vesicle-concentration-dependent rates were determined with the assumption that each LUV consists of

TABLE 2 Rate constants from kinetic experiments

Lipid Mixtures	k_{off} (s ⁻¹)	k_{on} (nM ⁻¹ s ⁻¹) per Vesicle	K_d (nM) per Vesicle	k_{on} ($\mu\text{M}^{-1}\text{s}^{-1}$) per Surface-Accessible Lipid Molecule	K_d (μM) per Surface-Accessible Lipid Molecule
LUVs 40% DOPS	209.0 \pm 10.8	9.0 \pm 3.7	23.3 \pm 10.8	0.42 \pm 0.17	497.6 \pm 223.9
LUVs 2% PtdIns3P	18.4 \pm 1.2	2.3 \pm 0.3	7.9 \pm 1.5	1.91 \pm 0.273	9.6 \pm 1.9
LUVs 2% PtdIns(3,5)P ₂	20.9 \pm 0.7	1.4 \pm 0.2	14.9 \pm 2.6	1.3 \pm 0.2	16.1 \pm 3.0
SUVs 2% PtdIns(3,5)P ₂	17.0 \pm 8.4	3.7 \pm 0.4	4.6 \pm 2.7	25.6 \pm 2.5	0.7 \pm 0.4
SUVs 2% PtdIns3P	14.1 \pm 10.6	3.4 \pm 0.5	4.1 \pm 3.8	23.4 \pm 3.5	0.6 \pm 0.5

Values and SE shown are from the best fits to data averaged over three to four repeated measurements for each condition.

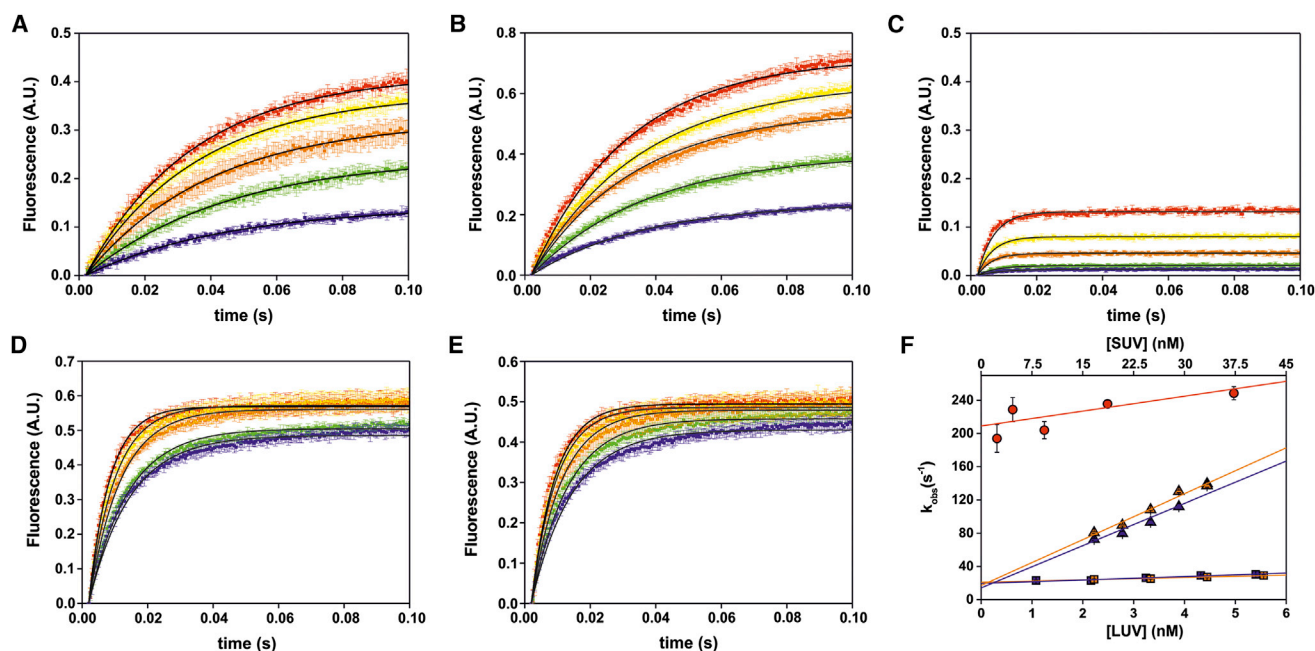


FIGURE 2 Kinetics of KIHsv2 binding to phospholipid vesicles. (A–E) Averaged time courses of dansyl emission at different vesicle concentrations. LUVs containing (A) DOPC/DOPE/PtdIns3P/dansyl-DHPE (73:20:2:5, molar ratio), (B) DOPC/DOPE/PtdIns(3,5)P₂/dansyl-DHPE (73:20:2:5, molar ratio), or (C) DOPC/DOPE/DOPS/dansyl-DHPE (35:20:40:5, molar ratio), or SUVs containing (D) DOPC/DOPE/PtdIns3P/dansyl-DHPE (73:20:2:5, molar ratio) or (E) DOPC/DOPE/PtdIns(3,5)P₂/dansyl-DHPE (73:20:2:5, molar ratio) were rapidly mixed with an equal volume of solution containing KIHsv2 (2 μ M). Solid lines show monoexponential fits. (F) Double x-scale graph showing the dependency of k_{obs} on vesicle concentration in the presence of LUVs containing DOPC/DOPE/PtdIns3P/dansyl-DHPE (blue squares), DOPC/DOPE/PtdIns(3,5)P₂/dansyl-DHPE (orange squares), or DOPC/DOPE/DOPS/dansyl-DHPE (red circles), and SUVs composed of DOPC/DOPE/PtdIns3P/dansyl-DHPE (blue triangles) or DOPC/DOPE/PtdIns(3,5)P₂/dansyl-DHPE (orange triangles). Error bars indicate the SE ($n = 3-4$). To see this figure in color, go online.

90,000 phospholipid molecules (30). KIHsv2 rapidly bound to 40% DOPS-containing LUVs with an apparent association constant per vesicle of $9.0 \pm 3.7 \text{ nM}^{-1}\text{s}^{-1}$ (Fig. 2; Table 2). This rate is nearly four to six times faster than the rate of binding to either 2% PtdIns3P- or 2% PtdIns(3,5)P₂-containing LUVs. These data indicate that the initial recruitment of PROPPINs to membranes is mediated by nonspecific electrostatic interactions. PIP binding then favors the retention of KIHsv2 at the membrane because the apparent dissociation rates are 10-fold lower for PIP-containing LUVs than for DOPS-containing vesicles. The dissociation constants per vesicle derived from the k_{on} and k_{off} values are $7.9 \pm 1.5 \text{ nM}$ for KIHsv2 binding to PtdIns3P LUVs, $14.9 \pm 2.6 \text{ nM}$ for PtdIns(3,5)P₂ binding, and $23.3 \pm 10.8 \text{ nM}$ for DOPS-containing LUVs.

When we normalize the association rates per surface-accessible PIP or DOPS molecule by assuming that 60% of the total lipids are localized on the liposome surface, we obtain a 5-fold lower association rate for KIHsv2 binding to DOPS in comparison with PtdIns3P (Table 2). The corresponding dissociation constants are $K_d = 16.1 \pm 3.0 \mu\text{M}$ for KIHsv2 binding to surface-accessible PtdIns(3,5)P₂, and $9.6 \pm 1.9 \mu\text{M}$ for PtdIns3P binding, whereas KIHsv2 bound DOPS with a 30- to 50-fold lower affinity. When we compared the dissociation constants per surface-access-

sible PIP molecules of LUVs and SUVs, we observed that KIHsv2 bound PIP-containing SUVs with an ~20 times higher affinity than LUVs. Thus, PROPPIN membrane binding is curvature dependent, with a preferred binding to strongly curved membranes.

Structure of the GS-linker KIHsv2 and analysis of loop 6CD mutants

To obtain better diffracting crystals than the primitive cubic wild-type KIHsv2 crystals, which diffracted to only 3.0 Å resolution (16), we replaced loop 6CD (residues 257–274) in KIHsv2 with a glycine-serine linker (GS)₄G. KIHsv2 ^{Δ loop6CD–GS} crystallized in the primitive hexagonal space group P3₁21 with one molecule in the asymmetric unit. The structure was determined at 2.8 Å resolution (Table S4). KIHsv2 ^{Δ loop6CD–GS} folds as a seven-bladed β -propeller as the wild-type protein, and both structures superimpose with a root mean-square deviation (RMSD) of 0.42 Å. The glycine-serine linker and loop 4CD are disordered in the KIHsv2 ^{Δ loop6CD–GS} structure. Although the crystals of the glycine-serine linker construct did not diffract significantly better than the wild-type KIHsv2 crystals, this structure confirms that the two PIP-binding sites are unaffected by a deletion of loop 6CD (Fig. 3, A and B).

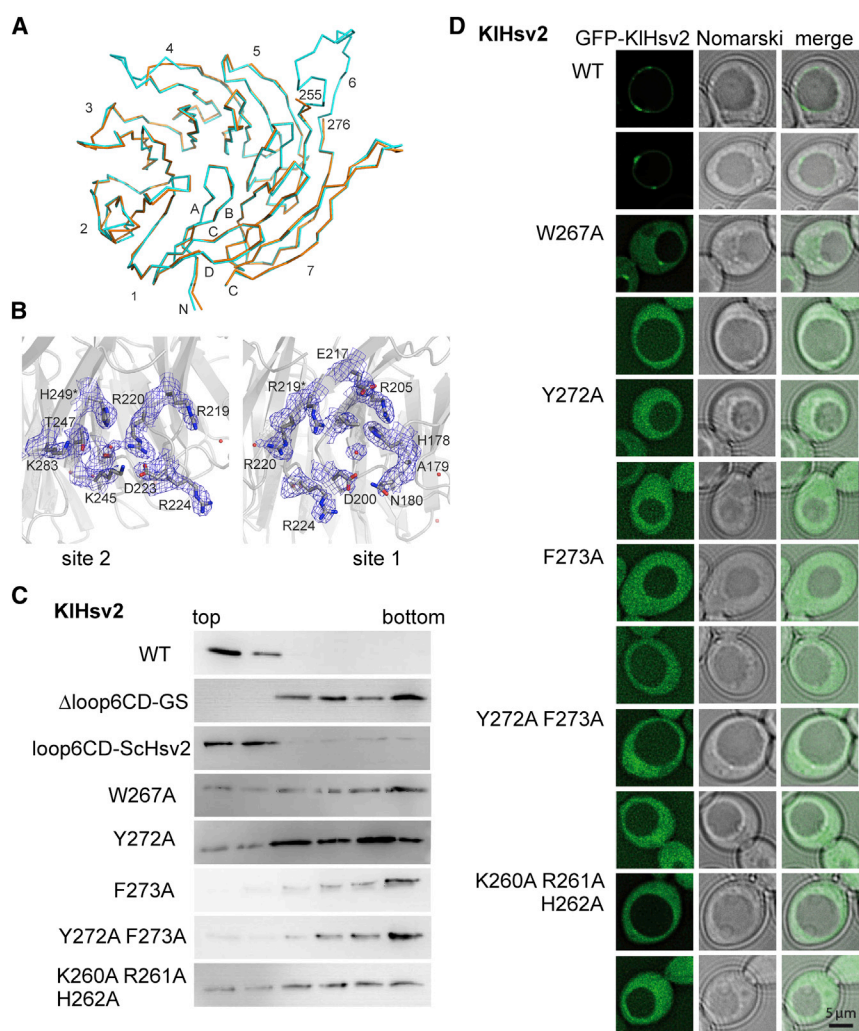


FIGURE 3 KIHsv2 Δ loop6CD-GS structure and mutagenesis studies of loop 6CD. (A) Superimposition of KIHsv2 Δ loop6CD-GS (orange, 4V16) and wild-type KIHsv2 (light blue, 4AV8) crystal structures. Blades 1–7 are marked. Each blade consists of four antiparallel β -strands, denoted as A–D beginning from the core. (B) Close-up of the two PIP-binding sites of KIHsv2 Δ loop6CD-GS, showing the 2.8 Å resolution 2mFo-DFc electron density map contoured at 1.0 σ (blue). The PIP-binding sites are on the rim of blades 4–6. The site 1 ScHsv2 R264A and site 2 ScHsv2 H294A mutants used for ITC measurements correspond to KIHsv2 residues R219 and H249, which are marked by asterisks. (C) Liposome flotation assays with KIHsv2 loop 6CD mutants. SUVs consisted of PC/PE/Texas-Red-PE/PIP (74:23:2:1, weight ratio) and proteins were used at a concentration of 1.5 μ M. (D) Fluorescence microscopy analysis of GFP-tagged KIHsv2 mutants. To see this figure in color, go online.

We analyzed membrane binding of KIHsv2 Δ loop6CD-GS by liposome flotation assays and found that binding was abolished (Fig. 3 C), which is consistent with the results of Baskaran et al. (17). We prepared a KIHsv2 $^{\Delta$ loop6CD-ScHsv2 construct in which loop 6CD was replaced with ScHsv2 loop 6CD, and found that liposome binding was retained in this chimeric construct.

Baskaran et al. (17) demonstrated that the KIHsv2 $^{W267A Y272A F273A}$ triple mutant does not bind to membranes. We analyzed the single aromatic to alanine mutants and the KIHsv2 $^{Y272A F273A}$ double mutant. The KIHsv2 Y272A and KIHsv2 W267A mutants showed decreased binding to liposomes. Membrane binding was abolished for KIHsv2 F273A and the KIHsv2 $^{Y272A F273A}$ double mutant. To analyze the importance of electrostatic interactions for membrane binding, we prepared a triple mutant KIHsv2 $^{K260A R261A H262A}$ in which three consecutive basic residues were mutated. Liposome binding of this triple mutant was diminished.

We further analyzed the cellular localization of the KIHsv2 point mutants. N-terminal GFP-tagged wild-type

KIHsv2 and the KIHsv2 point mutants were expressed in *S. cerevisiae* and analyzed by fluorescence microscopy (Fig. 3 D). Wild-type GFP-KIHsv2 localized to the vacuole membrane and perivacuolar structures. In contrast, the KIHsv2 mutants predominantly localized to the cytosol due to a loss of membrane binding. Based on the results of the in vivo and in vitro studies, we conclude that both hydrophobic and electrostatic interactions are important for membrane binding of loop 6CD.

MD simulations

To gain further insights into how loop 6CD interacts with the membrane, we performed MD simulations based on the KIHsv2 crystal structure. We applied a previously published protocol for CG-MD simulations in which a lipid bilayer is assembled around the exposed hydrophobic parts of a protein (41). This method has the advantage that it yields an unbiased orientation of the protein toward the membrane. Four atoms are approximated to a bead in CG-MD simulations. Therefore, each amino acid is represented

by one backbone bead and side-chain particle(s) depending on the size of the residue. PIPs cannot be modeled accurately because of these approximations.

Initially, dipalmitoyl-phosphatidylcholine (DPPC) molecules are randomly positioned in a water box with the protein at the center. During the first 10 ns, the lipid bilayer forms around loop 6CD (Fig. 4 A; Movie S1, the first 45 ns). The protein binds in a tilted orientation to the membrane and loop 6CD does not penetrate the membrane deeper than the hydrophilic layer. The level of insertion does not change throughout the remaining 90 ns of the simulation, during which the protein mainly rotates freely around the loop.

In less than half of the CG-MD runs, we observed lipid bilayer formation, likely due to the high water/lipid ratio. The high solvent content reflects the fact that a large simulation box was needed to fit the protein. The box size of the system was kept small to avoid a further increase in the water/lipid ratio and thus facilitate lipid bilayer formation. Because this might lead to a tilted orientation of the protein, we then placed the protein-membrane system in a bigger box by increasing the *z* axis to 12 nm, and performed a 1 μ s CG-MD (Fig. 4 B; Movie S2, the first 96 ns). The average tilt angle was $\sim 30^\circ$ (Fig. S3 A).

The degree of membrane penetration of loop 6CD might be underestimated due to the limitations of CG-MD simulations, i.e., the constraints on the secondary structure of the protein and an underestimation of the polarity effects between water and the membrane (42). Also, the conformation of loop 6CD might differ between solution and the membrane environment, which cannot be accounted for in a CG-MD simulation, because loop conformations are locked. To address these points, we performed atomistic MD simulations of the protein-membrane system and the free protein. These MD simulations show that loop 6CD is more flexible in solution than when it is membrane bound (Fig. S3 D).

The time course of the 100 ns protein-membrane MD simulation is shown in Fig. 4 C (Movie S3). During the simulation, loop 6CD penetrates deeper into the membrane, while the protein tumbles around this loop, bringing the two FRRG arginines in proximity to the membrane. To quantify the interactions, we calculated the number of contacts made by each amino acid with the hydrophobic core of the membrane per picosecond (Fig. S3, B and C). Blades 4 and 5 are in contact with the lipid bilayer (Fig. S3, B and C). Loop 6CD is the region of the protein that has most contacts with the hydrophobic part of the membrane and inserts most deeply into the lipid bilayer, functioning like an anchor for membrane binding of PROPPINs. This anchor is highly flexible in solution, but its flexibility decreases upon membrane insertion (Fig. S3 D). This simulation further shows that a large portion of the surface of the protein remains accessible for protein-protein interactions.

DISCUSSION

We combined ITC, stopped-flow measurements, MD simulations, x-ray crystallography, and in vivo and in vitro mutagenesis studies for an in-depth characterization of PROPPIN-membrane binding. Our ITC measurements show that binding is enthalpy driven and that PROPPINs bind with a nanomolar to low-micromolar affinity to liposome-incorporated PtdIns3P and PtdIns(3,5)P₂. PROPPINs have two PIP-binding sites (16–18), and our measured stoichiometries range from 1.4 to 3.3 for PIP-to-PROPPIN binding. We repeated earlier ITC measurements with ScHsv2 and PtdIns3P to directly compare them with the measurements of the site 1 ScHsv2^{R264A} and site 2 ScHsv2^{H294A} mutants. We previously reported a K_d of $0.67 \pm 0.04 \mu\text{M}$ for wild-type ScHsv2 (16), which compares to $0.40 \pm 0.05 \mu\text{M}$ for PtdIns3P binding obtained in this study. The ScHsv2^{R264A} and ScHsv2^{H294A} mutants,

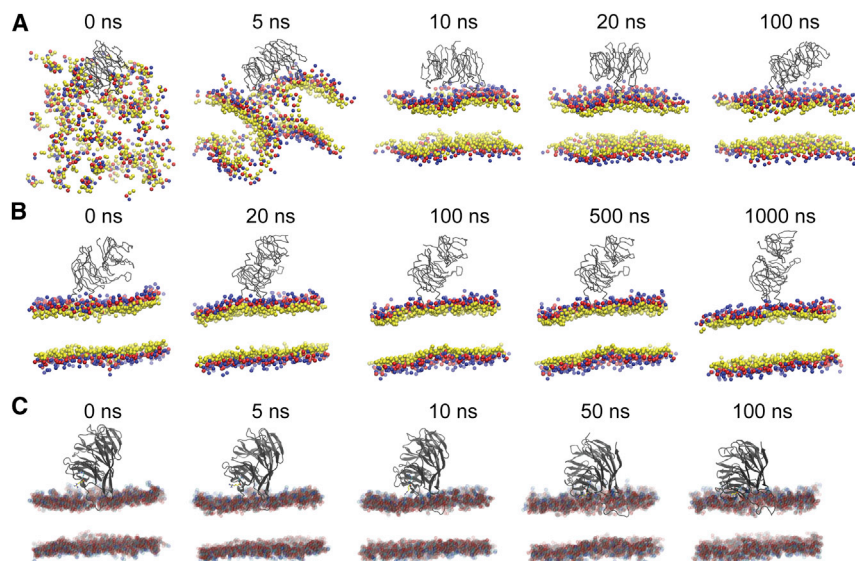


FIGURE 4 CG and atomistic MD simulations. (A) Time course of a 100 ns CG-MD simulation of DPPC bilayer formation around KIHsv2. DPPC choline groups are represented in blue, phosphates are red, and glycerol groups are yellow. For simplicity, water molecules and hydrophobic chains of the lipids are not shown. (B) Time course of a 1 μ s CG-MD simulation of KIHsv2 in a DPPC membrane. (C) A 100 ns atomistic MD simulation of KIHsv2 in a DPPC membrane. The oxygen atoms of the DPPC are represented in red, nitrogens are dark blue, phosphorous is brown, carbons are light blue, FRRG arginine R219 is yellow, and R220 is blue. To see this figure in color, go online.

both of which have only a single functional PIP-binding site, bound much more weakly, with dissociation constants of $10.9 \pm 1.2 \mu\text{M}$ and $5.9 \pm 1.6 \mu\text{M}$, respectively. The low affinities of the single PIP-binding sites explain the need for the two PIP sites in PROPPINs. This is comparable to the FYVE domain, which needs two PtdIns3P-binding sites for high-affinity binding and achieves it through dimerization, whereas PROPPINs contain two PIP-binding sites in a single domain (43,44).

In our ITC measurements, PROPPINs bind with a higher affinity to PtdIns(3,5)P₂ than to PtdIns3P with the exception of K1Atg21, which has similar affinities for both PIPs with dissociation constants of $0.86 \pm 0.18 \mu\text{M}$ for PtdIns3P and $1.14 \pm 0.29 \mu\text{M}$ for PtdIns(3,5)P₂, respectively. We determined a K_d of $110 \pm 10 \text{ nM}$ for PtdIns(3,5)P₂ binding of PaAtg18. This value is in agreement with an earlier study that reported a K_d of 180 nM for PtdIns(3,5)P₂ binding of GST-ScAtg18 as determined by surface plasmon resonance measurements using chips covered with 3% PtdIns(3,5)P₁₂-containing vesicles (2).

Baskaran et al. (17) observed submicromolar affinities of K1Hsv2 binding to PtdIns3P and PtdIns(3,5)P₂ containing dansyl-labeled LUVs in a FRET-based assay. Here, we determined dissociation constants per surface-accessible PIP molecule of $9.6 \pm 1.9 \mu\text{M}$ for 2% PtdIns3P-containing LUVs and $16.1 \pm 3.0 \mu\text{M}$ for PtdIns(3,5)P₂-containing LUVs by stopped-flow measurements. Different liposome lipid compositions were used in the two studies, which has an effect on the measured affinities. Our LUVs consisted of 2% PIP and the neutral lipids PC and PE, whereas the LUVs used by Baskaran et al. (17) contained 5% PIP and 55–60% PS in addition to PC and PE.

ITC measurements with K1Hsv2 and PIP-containing SUVs yielded dissociation constants of $0.50 \pm 0.07 \mu\text{M}$ for PtdIns3P binding and $0.18 \pm 0.02 \mu\text{M}$ for the interaction with PtdIns(3,5)P₂, respectively. These values are comparable to the stopped-flow measurements obtained using these SUVs. The dissociation constant per surface-accessible PIP molecule is $0.6 \pm 0.5 \mu\text{M}$ for PtdIns3P-containing SUVs; however, lower-affinity binding was observed for PtdIns(3,5)P₂ SUVs, with a K_d of $0.7 \pm 0.4 \mu\text{M}$. When comparing the results of the ITC and stopped-flow measurements, one has to consider that both techniques differ in their detection modes. During ITC, heat changes upon binding are directly measured, whereas in the FRET-based assay, the readout of PIP binding is indirect through FRET emission of the vesicle-incorporated dansyl dye.

Stopped-flow measurements allowed us to directly compare SUV and LUV binding of PROPPINs. However, the LUVs and SUVs were prepared by different methods. LUVs were made by extrusion through filters with a pore size of 100 nm. In contrast, SUVs were prepared by dissolving the dried lipid film in 3% sodium cholate containing HP150 buffer. The cholate concentration (70 mM) is above the critical micelle concentration (9–15 mM). SUVs then

form through removal of the detergent by gel filtration. We do not know how much cholate remains in these SUVs. However, earlier multi-angle laser light scattering measurements showed that SUV preparations are homogeneous, with an average diameter of 36 nm (26), in agreement with our dynamic light scattering data, which yielded radii of $16.7 \pm 11.1 \text{ nm}$ for PtdIns3P-containing SUVs and $20.0 \pm 9.6 \text{ nm}$ for PtdIns(3,5)P₂-containing SUVs (Fig. S2). Hence, we assume that the remaining cholate most probably has no detrimental effect on SUV stability.

In our stopped-flow measurements, K1Hsv2 bound with an ~20-fold higher affinity to SUVs than to LUVs with the same lipid compositions. We conclude that PROPPIN-membrane binding is curvature dependent and that PROPPINs bind with a higher affinity to strongly curved membranes. A number of lipid-binding proteins are known to be sensitive to membrane curvature (45,46), including synaptotagmin and sorting nexin-1, which also preferentially bind smaller liposomes (47,48).

We gained further insights into the kinetics of PROPPIN phospholipid binding through the stopped-flow measurements. K1Hsv2 bound with an ~4- to 6-fold higher apparent association rate to 40% DOPS-containing LUVs than to PIP-LUVs. However, the dissociation rate was 10 times slower for the PIP-containing vesicles than for the DOPS-LUVs. These data are consistent with the notion that an initial membrane targeting of PROPPINs occurs through nonspecific electrostatic interactions and the protein is then retained at the membrane through PIP binding.

In addition to our experimental work, we performed MD simulations with K1Hsv2 to further study PROPPIN-membrane interactions. First, we performed CG-MD self-assembly simulations to obtain an unbiased insertion of the protein into the lipid bilayer (41). These calculations served as a starting point for atomistic MD simulations. All MD simulations were done with PC and contained no PIPs, thus showing membrane-K1Hsv2 interactions without PIP binding. Loop 6CD interacts with the lipids of the upper leaflet of the bilayer and is the region of the protein that inserts most deeply into the membrane. The importance of loop 6CD for membrane binding of PROPPINs was demonstrated earlier when a replacement of loop 6CD by a glycine-serine linker abolished membrane binding of PROPPINs (17).

Our K1Hsv2^{Δloop6CD-GS} structure shows that loss of membrane binding is due to the deletion of loop 6CD alone, because the two PIP-binding sites were not affected by this substitution. Both hydrophobic and electrostatic interactions are important for loop 6CD membrane binding. The triple mutant K1Hsv2^{K260A R261A H262A} showed decreased binding in liposome flotation assays and cytoplasmic localization in *S. cerevisiae*. The two aromatic loop 6CD mutants K1Hsv2^{Y272A} and K1Hsv2^{F273A} lost membrane association in cellular localization studies and showed either decreased (Y272A) or no binding (F273A) to SUVs in liposome

flotation assays. Likewise, a tetra-alanine mutant of hydrophobic residues from the four membrane insertion loops of the synaptotagmin C2A and C2B domains showed diminished SUV binding in comparison with the wild-type protein (47). A possible explanation for the higher-affinity SUV binding of PROPPINs is that strongly bent membranes may facilitate loop 6CD insertion.

Membrane binding of proteins can be regulated by phosphorylation. For instance, phosphorylation mediates the cell-cycle-dependent membrane localization of the nuclear mitotic apparatus protein NuMa (49). Likewise, in an analysis of *Pichia pastoris* Atg18 (PpAtg18), Tamura et al. (19) showed that the phosphorylation of loops 6CD and 7AB has an influence on membrane targeting of the protein. Dephosphorylation facilitates vacuolar membrane binding of PpAtg18. The authors further observed that phosphorylation of PpAtg18 increases during oxidative stress, which might help the cell to adapt to environmental stress conditions (19). PpAtg18 loop 6CD residues S388 and S391, which become phosphorylated, are not conserved in PROPPINs. In fact, loop 6CD is one of the least conserved regions and varies in length among PROPPIN family members (Fig. S1). However, analysis with NetPhosYeast (50) indicates the presence of phosphorylation sites in other PROPPINs as well, such as S278 in KIHsv2 loop 6CD and the corresponding residue S340 in ScHsv2. Variations in the number of loop 6CD phosphorylation sites with potentially different kinase specificities might differently affect membrane targeting of the individual PROPPIN family members.

We propose a model in which PROPPINs are initially targeted to membranes through nonspecific electrostatic interactions. PROPPINs are then retained in the membrane through PIP binding to the two sites and membrane insertion of loop 6CD. This mechanism is in agreement with membrane binding of other PIP-binding proteins, where proteins first associate with the membrane through electrostatic interactions, and then more tightly bound complexes are formed through hydrogen-bond formation and electrostatic interactions with PIP headgroups and membrane insertion (51).

How is specific membrane targeting of PROPPINs achieved in vivo? First, binding of two PIP molecules is required for high-affinity membrane association. Atg18 localizes to the PtdIns3P-containing PAS (the isolation membrane from which autophagosomes form), endosomes, and PtdIns(3,5)P₂-containing vacuolar membranes (2,6–8,52). However, although Atg21 binds PtdIns(3,5)P₂ with high affinity, so far no PtdIns(3,5)P₂-dependent function has been described for this protein. PROPPINs do not localize to cellular membranes that do not contain PtdIns3P or PtdIns(3,5)P₂, such as the plasma membrane, which contains PtdIns(4,5)P₂ and PtdIns(3,4,5)P₃ and is enriched in anionic phospholipids (51,53,54). Second, as discussed previously (19), phosphorylation of the membrane insertion loop 6CD and loop 7AB has a regulatory role in membrane targeting.

Third, protein-protein interactions are important for the localization of PROPPINs. Atg18 forms a complex with Atg2, which is essential for autophagosome formation (55). Atg2 is required for PAS targeting of Atg18 (56). Although an earlier study showed that Atg18 PIP binding is required for Atg2-Atg18 targeting to the PAS (55), an interdependency of Atg2 and Atg18 to PAS targeting was also reported, which further supports a role of Atg2 in Atg18 localization (57). At the vacuole, Atg18 is part of a large complex that regulates PtdIns(3,5)P₂ levels. The complex consists of the scaffold protein Vac14, the PtdIns3P 5'-kinase Fab1, the PtdIns(3,5)P₂-specific 5'-phosphatase Fig. 4, the Fab1 activator Vac7, and Atg18, which acts as a Fab1 inhibitor (12,13). Vac7 contributes to the recruitment of Atg18 to vacuolar membranes, providing another example of the role of protein-protein interactions in PROPPIN targeting (13).

Lastly, our observation that PROPPINs bind SUVs with a higher affinity than they bind LUVs suggests that membrane curvature might also influence protein localization in vivo. Recently, Suzuki et al. (52) fine mapped the localization of yeast autophagy proteins on the isolation membrane using fluorescence microscopy, and found that Atg18 localizes to the strongly bent edges of the isolation membrane. Preferential binding of PROPPINs to highly curved membrane regions, as observed in our stopped-flow measurements, would explain this localization pattern.

CONCLUSIONS

PROPPINs are peripheral membrane proteins that achieve high-affinity binding through two PIP-binding sites and a membrane insertion loop, all within a single domain. Our data are consistent with a model in which PROPPINs are targeted to membranes through nonspecific electrostatic interactions to acidic phospholipids. PIP binding then retains the protein at the membrane and is a key factor in achieving site-specific binding. Mutation of one PIP-binding site reduces PIP affinity by 15- to 30-fold, explaining the requirement for two PIP-binding sites in PROPPINs. Membrane binding of PROPPINs is curvature dependent because PROPPINs bind SUVs with a higher affinity than they bind LUVs. The two PIP-binding sites act in concert with loop 6CD. Deletion of loop 6CD abolishes membrane binding, but does not affect the PIP sites visible in the KIHsv2 loop 6CD deletion glycine-serine linker crystal structure. MD simulations show that loop 6CD is the region of the protein that inserts most deeply into the membrane, leaving a large portion of the surface accessible for the assembly of PROPPIN-protein complexes.

SUPPORTING MATERIAL

Supporting Materials and Methods, three figures, four tables, and three movies are available at [http://www.biophysj.org/biophysj/supplemental/S0006-3495\(15\)00307-0](http://www.biophysj.org/biophysj/supplemental/S0006-3495(15)00307-0).

AUTHOR CONTRIBUTIONS

R.A.B., A.S., R.K., A.P.-L., and K.K. performed research. M.T. and K.K. designed research. All authors analyzed data. A.S. and K.K. wrote the manuscript with contributions from all authors.

ACKNOWLEDGMENTS

Diffraction data were collected at beamline X10SA (Swiss Light Source, Paul Scherrer Institute, Villigen, Switzerland). We thank the beamline staff for their help during data collection. We also thank Prof. M. Müller for a valuable discussion regarding MD simulations, U. Ries for determining phosphate concentrations, and Prof. R. Jahn for his generous support.

This work was funded by the DFG (SFB860 to M.T. and K.K.).

REFERENCES

- Dove, S. K., K. Dong, ..., R. H. Michell. 2009. Phosphatidylinositol 3,5-bisphosphate and Fab1p/PIKfyve underpin endo-lysosome function. *Biochem. J.* 419:1–13.
- Dove, S. K., R. C. Piper, ..., M. A. Lemmon. 2004. Svp1p defines a family of phosphatidylinositol 3,5-bisphosphate effectors. *EMBO J.* 23:1922–1933.
- Strømhaug, P. E., F. Reggiori, ..., D. J. Klionsky. 2004. Atg21 is a phosphoinositide binding protein required for efficient lipidation and localization of Atg8 during uptake of aminopeptidase I by selective autophagy. *Mol. Biol. Cell.* 15:3553–3566.
- Krick, R., J. Tolstrup, ..., M. Thumm. 2006. The relevance of the phosphatidylinositolphosphat-binding motif FRRGT of Atg18 and Atg21 for the Cvt pathway and autophagy. *FEBS Lett.* 580:4632–4638.
- Barth, H., K. Meiling-Wesse, ..., M. Thumm. 2001. Autophagy and the cytoplasm to vacuole targeting pathway both require Aut10p. *FEBS Lett.* 508:23–28.
- Guan, J., P. E. Stromhaug, ..., D. J. Klionsky. 2001. Cvt18/Gsa12 is required for cytoplasm-to-vacuole transport, pexophagy, and autophagy in *Saccharomyces cerevisiae* and *Pichia pastoris*. *Mol. Biol. Cell.* 12:3821–3838.
- Reggiori, F., K. A. Tucker, ..., D. J. Klionsky. 2004. The Atg1-Atg13 complex regulates Atg9 and Atg23 retrieval transport from the pre-autophagosomal structure. *Dev. Cell.* 6:79–90.
- Krick, R., S. Henke, ..., M. Thumm. 2008. Dissecting the localization and function of Atg18, Atg21 and Ygr223c. *Autophagy.* 4:896–910.
- Polson, H. E., J. de Lartigue, ..., S. A. Tooze. 2010. Mammalian Atg18 (WIPI2) localizes to omegasome-anchored phagophores and positively regulates LC3 lipidation. *Autophagy.* 6:506–522.
- Dooley, H. C., M. Razi, ..., S. A. Tooze. 2014. WIPI2 links LC3 conjugation with PI3P, autophagosome formation, and pathogen clearance by recruiting Atg12-5-16L1. *Mol. Cell.* 55:238–252.
- Krick, R., Y. Muehe, ..., M. Thumm. 2008. Piecemeal microautophagy of the nucleus requires the core macroautophagy genes. *Mol. Biol. Cell.* 19:4492–4505.
- Jin, N., C. Y. Chow, ..., L. S. Weisman. 2008. VAC14 nucleates a protein complex essential for the acute interconversion of PI3P and PI(3,5)P(2) in yeast and mouse. *EMBO J.* 27:3221–3234.
- Efe, J. A., R. J. Botelho, and S. D. Emr. 2007. Atg18 regulates organelle morphology and Fab1 kinase activity independent of its membrane recruitment by phosphatidylinositol 3,5-bisphosphate. *Mol. Biol. Cell.* 18:4232–4244.
- Meiling-Wesse, K., H. Barth, ..., M. Thumm. 2004. Atg21 is required for effective recruitment of Atg8 to the preautophagosomal structure during the Cvt pathway. *J. Biol. Chem.* 279:37741–37750.
- Juris, L., M. Montino, ..., R. Krick. 2015. PI3P binding by Atg21 organises Atg8 lipidation. *EMBO J.* 34:955–973.
- Krick, R., R. A. Busse, ..., K. Kühnel. 2012. Structural and functional characterization of the two phosphoinositide binding sites of PROPPINs, a β -propeller protein family. *Proc. Natl. Acad. Sci. USA.* 109:E2042–E2049.
- Baskaran, S., M. J. Ragusa, ..., J. H. Hurley. 2012. Two-site recognition of phosphatidylinositol 3-phosphate by PROPPINs in autophagy. *Mol. Cell.* 47:339–348.
- Watanabe, Y., T. Kobayashi, ..., N. N. Noda. 2012. Structure-based analyses reveal distinct binding sites for Atg2 and phosphoinositides in Atg18. *J. Biol. Chem.* 287:31681–31690.
- Tamura, N., M. Oku, ..., Y. Sakai. 2013. Atg18 phosphoregulation controls organellar dynamics by modulating its phosphoinositide-binding activity. *J. Cell Biol.* 202:685–698.
- Studier, F. W. 2005. Protein production by auto-induction in high density shaking cultures. *Protein Expr. Purif.* 41:207–234.
- Kabsch, W. 1993. Automatic processing of rotation diffraction data from crystals of initially unknown symmetry and cell constants. *J. Appl. Cryst.* 26:795–800.
- Vagin, A., and A. Teplyakov. 2010. Molecular replacement with MOLREP. *Acta Crystallogr. D Biol. Crystallogr.* 66:22–25.
- Adams, P. D., P. V. Afonine, ..., P. H. Zwart. 2010. PHENIX: a comprehensive Python-based system for macromolecular structure solution. *Acta Crystallogr. D Biol. Crystallogr.* 66:213–221.
- Emsley, P., and K. Cowtan. 2004. Coot: model-building tools for molecular graphics. *Acta Crystallogr. D Biol. Crystallogr.* 60:2126–2132.
- Schrödinger, LLC. 2010. The PyMOL Molecular Graphics System, version 1.3r1.
- Busse, R. A., A. Scacioc, ..., K. Kühnel. 2013. Qualitative and quantitative characterization of protein-phosphoinositide interactions with liposome-based methods. *Autophagy.* 9:770–777.
- Schuetz, C. G., K. Hatsuzawa, ..., R. Jahn. 2004. Determinants of liposome fusion mediated by synaptic SNARE proteins. *Proc. Natl. Acad. Sci. USA.* 101:2858–2863.
- Eibl, H., and W. E. Lands. 1969. A new, sensitive determination of phosphate. *Anal. Biochem.* 30:51–57.
- Pérez-Lara, A., A. L. Egea-Jiménez, ..., J. C. Gómez-Fernández. 2012. The membrane binding kinetics of full-length PKC α is determined by membrane lipid composition. *Biochim. Biophys. Acta.* 1821:1434–1442.
- Arbuzova, A., J. Wang, ..., S. McLaughlin. 1997. Kinetics of interaction of the myristoylated alanine-rich C kinase substrate, membranes, and calmodulin. *J. Biol. Chem.* 272:27167–27177.
- Nalefski, E. A., and A. C. Newton. 2001. Membrane binding kinetics of protein kinase C β II mediated by the C2 domain. *Biochemistry.* 40:13216–13229.
- Niedenthal, R. K., L. Riles, ..., J. H. Hegemann. 1996. Green fluorescent protein as a marker for gene expression and subcellular localization in budding yeast. *Yeast.* 12:773–786.
- Hess, B., C. Kutzner, ..., E. Lindahl. 2008. GROMACS 4: algorithms for highly efficient, load-balanced, and scalable molecular simulation. *J. Chem. Theory Comput.* 4:435–447.
- Van Der Spoel, D., E. Lindahl, ..., H. J. C. Berendsen. 2005. GRO-MACS: fast, flexible, and free. *J. Comput. Chem.* 26:1701–1718.
- Brocos, P., P. Mendoza-Espinosa, ..., A. Pineiro. 2012. Multiscale molecular dynamics simulations of micelles: coarse-grain for self-assembly and atomic resolution for finer details. *Soft Matter.* 8:9005–9014.
- Oostenbrink, C., A. Villa, ..., W. F. van Gunsteren. 2004. A biomolecular force field based on the free enthalpy of hydration and solvation: the GROMOS force-field parameter sets 53A5 and 53A6. *J. Comput. Chem.* 25:1656–1676.
- Berger, O., O. Edholm, and F. Jähnig. 1997. Molecular dynamics simulations of a fluid bilayer of dipalmitoylphosphatidylcholine at full hydration, constant pressure, and constant temperature. *Biophys. J.* 72:2002–2013.

38. Hermans, J., H. J. C. Berendsen, ..., J. P. M. Postma. 1984. A consistent empirical potential for water-protein interactions. *Biopolymers*. 23:1513–1518.
39. Humphrey, W., A. Dalke, and K. Schulten. 1996. VMD: visual molecular dynamics. *J. Mol. Graph.* 14:33–38, 27–28.
40. Vennekate, W., S. Schröder, ..., P. J. Walla. 2012. Cis- and trans-membrane interactions of synaptotagmin-1. *Proc. Natl. Acad. Sci. USA*. 109:11037–11042.
41. Balali-Mood, K., P. J. Bond, and M. S. P. Sansom. 2009. Interaction of monotopic membrane enzymes with a lipid bilayer: a coarse-grained MD simulation study. *Biochemistry*. 48:2135–2145.
42. Yesylevskyy, S. O., L. V. Schäfer, ..., S. J. Marrink. 2010. Polarizable water model for the coarse-grained MARTINI force field. *PLOS Comput. Biol.* 6:e1000810.
43. Hayakawa, A., S. J. Hayes, ..., S. Corvera. 2004. Structural basis for endosomal targeting by FYVE domains. *J. Biol. Chem.* 279:5958–5966.
44. Dumas, J. J., E. Merithew, ..., D. G. Lambright. 2001. Multivalent endosome targeting by homodimeric EEA1. *Mol. Cell*. 8:947–958.
45. He, J., R. M. Haney, ..., T. G. Kutateladze. 2008. Molecular mechanism of membrane targeting by the GRP1 PH domain. *J. Lipid Res.* 49:1807–1815.
46. Lemmon, M. A. 2008. Membrane recognition by phospholipid-binding domains. *Nat. Rev. Mol. Cell Biol.* 9:99–111.
47. Martens, S., M. M. Kozlov, and H. T. McMahon. 2007. How synaptotagmin promotes membrane fusion. *Science*. 316:1205–1208.
48. Carlton, J., M. Bujny, ..., P. J. Cullen. 2004. Sorting nexin-1 mediates tubular endosome-to-TGN transport through coincidence sensing of high- curvature membranes and 3-phosphoinositides. *Curr. Biol.* 14:1791–1800.
49. Zheng, Z., Q. Wan, ..., Q. Du. 2014. Cell cycle-regulated membrane binding of NuMA contributes to efficient anaphase chromosome separation. *Mol. Biol. Cell*. 25:606–619.
50. Ingrell, C. R., M. L. Miller, ..., N. Blom. 2007. NetPhosYeast: prediction of protein phosphorylation sites in yeast. *Bioinformatics*. 23:895–897.
51. Stahelin, R. V., J. L. Scott, and C. T. Frick. 2014. Cellular and molecular interactions of phosphoinositides and peripheral proteins. *Chem. Phys. Lipids*. 182:3–18.
52. Suzuki, K., M. Akioka, ..., Y. Ohsumi. 2013. Fine mapping of autophagy-related proteins during autophagosome formation in *Saccharomyces cerevisiae*. *J. Cell Sci.* 126:2534–2544.
53. McLaughlin, S., and D. Murray. 2005. Plasma membrane phosphoinositide organization by protein electrostatics. *Nature*. 438:605–611.
54. Heo, W. D., T. Inoue, ..., T. Meyer. 2006. PI(3,4,5)P3 and PI(4,5)P2 lipids target proteins with polybasic clusters to the plasma membrane. *Science*. 314:1458–1461.
55. Obara, K., T. Sekito, ..., Y. Ohsumi. 2008. The Atg18-Atg2 complex is recruited to autophagic membranes via phosphatidylinositol 3-phosphate and exerts an essential function. *J. Biol. Chem.* 283:23972–23980.
56. Rieter, E., F. Vinke, ..., F. Reggiori. 2013. Atg18 function in autophagy is regulated by specific sites within its β -propeller. *J. Cell Sci.* 126: 593–604.
57. Suzuki, K., Y. Kubota, ..., Y. Ohsumi. 2007. Hierarchy of Atg proteins in pre-autophagosomal structure organization. *Genes Cells*. 12: 209–218.